



# Density Profiles of Collapsed Rotating Massive Stars Favor Long Gamma-Ray Bursts

Goni Halevi<sup>1,2</sup> , Belinda Wu<sup>1</sup>, Philipp Mösta<sup>3</sup> , Ore Gottlieb<sup>4</sup> , Alexander Tchekhovskoy<sup>4</sup> , and David R. Aguilera-Dena<sup>5</sup> <sup>1</sup> Department of Astrophysical Sciences, Princeton University, 4 Ivy Lane, Princeton, NJ 08544, USA; [ghalevi@princeton.edu](mailto:ghalevi@princeton.edu)<sup>2</sup> Institute For Advanced Study, 1 Einstein Drive, Princeton, NJ 08540, USA<sup>3</sup> GRAPPA, Anton Pannekoek Institute for Astronomy, Institute of High-Energy Physics, and Institute of Theoretical Physics, University of Amsterdam, Science Park 904, 1098 XH Amsterdam, The Netherlands<sup>4</sup> Center for Interdisciplinary Exploration & Research in Astrophysics (CIERA), Physics & Astronomy, Northwestern University, Evanston, IL 60201, USA<sup>5</sup> Institute of Astrophysics, FORTH, Dept. of Physics, University of Crete, Voutes, University Campus, GR-71003 Heraklion, Greece

Received 2022 November 21; revised 2023 January 18; accepted 2023 January 29; published 2023 February 17

## Abstract

Long-duration gamma-ray bursts (IGRBs) originate in relativistic collimated outflows—jets—that drill their way out of collapsing massive stars. Accurately modeling this process requires realistic stellar profiles for the jets to propagate through and break out of. Most previous studies have used simple power laws or pre-collapse models for massive stars. However, the relevant stellar profile for IGRB models is in fact that of a star after its core has collapsed to form a compact object. To self-consistently compute such a stellar profile, we use the open-source code GR1D to simulate the core-collapse process for a suite of low-metallicity rotating massive stellar progenitors that have undergone chemically homogeneous evolution. Our models span a range of zero-age main-sequence (ZAMS) masses:  $M_{\text{ZAMS}} = 13, 18, 21, 25, 35, 40,$  and  $45M_{\odot}$ . All of these models, at the onset of core-collapse, feature steep density profiles,  $\rho \propto r^{-\alpha}$ , with  $\alpha \approx 2.5$ , which would result in jets that are inconsistent with IGRB observables. We follow the collapses of four of the seven models until they form black holes (BHs) and the other three models until they form proto-neutron stars (PNSs). We find, across all models, that the density profile outside the newly formed BH or PNS is well represented by a flatter power law with  $\alpha \approx 1.35\text{--}1.55$ . Such flat density profiles are conducive to the successful formation and breakout of BH-powered jets and are, in fact, required to reproduce observable properties of IGRBs. Future models of IGRBs should be initialized with shallower post-collapse stellar profiles, like those presented here, instead of the much steeper pre-collapse profiles that are typically used.

*Unified Astronomy Thesaurus concepts:* [Hydrodynamical simulations \(767\)](#); [General relativity \(641\)](#); [Stellar mass black holes \(1611\)](#); [Gamma-ray bursts \(629\)](#); [Core-collapse supernovae \(304\)](#)

## 1. Introduction

Evolved massive stars that undergo core collapse are commonly accepted as the progenitors of luminous energetic transient sources, including long-duration gamma-ray bursts (IGRBs) and core-collapse supernova (CCSN) explosions. The environments of IGRBs—star-forming and preferentially low-metallicity galaxies—suggest a link to the core-collapse process (e.g., Bloom et al. 2002). Individual IGRBs that have been detected as being coincident with broad-lined Type Ic (Ic-bl) SNe (e.g., Galama et al. 1998; Modjaz et al. 2006), hydrogen- and helium-deficient explosions with broad spectral features, bolster the “SN–GRB” connection between the central engines driving these events (Modjaz et al. 2016). One of the favored models for the engine of IGRBs is the collapsar scenario (MacFadyen & Woosley 1999). Under this framework, the iron core of a massive star collapses to a Kerr black hole (BH), without driving a successful SN explosion. Afterward, the high angular momentum of the stellar envelope leads to disk formation, and the BH accretes matter, enabling energy to be extracted as the Poynting flux (Blandford & Znajek 1977; Komissarov & Barkov 2009). This process leads to the launching of a relativistic collimated outflow—a jet—that clears its path out of the star and breaks out of the

envelope, to eventually be observed as a burst of beamed energetic gamma-rays.

Evolved massive stripped-envelope stars, such as Wolf–Rayet (W-R) stars, are theoretically the most likely evolutionary channel to lead to collapsars, as their significant wind-driven mass loss results in depleted stellar envelopes for jets to break out of (Woosley 1993). Stripped-envelope stars are also associated with SNe that lack strong hydrogen or helium features in their spectra—Type Ic SNe (e.g., Gal-Yam et al. 2014; Dessart et al. 2017). This same class of SN has been observationally linked to IGRBs, suggesting that W-Rs or other stripped-envelope stars are the progenitors of IGRBs. These stars may include ones that have undergone chemically homogeneous evolution (CHE) without developing the optically thick winds that are characteristic of W-Rs, which are observationally distinguished by their emission lines (e.g., Szécsi et al. 2015; Aguilera-Dena et al. 2022). Massive stripped-envelope stars that fail to form BHs may also successfully power IGRBs and Type Ic-bl SNe through the protomagnetar model (Metzger et al. 2011; Shankar et al. 2021; Song & Liu 2023). Simulations have suggested that the central engine of an IGRB can itself trigger a Type Ic-bl SN in a W-R star, jointly producing both of the observed phenomena from the same massive stellar progenitor (Barnes et al. 2018), but others have found that the quasi-spherical explosion and beamed relativistic emission instead require two distinct energy channels (Eisenberg et al. 2022).

A subset of SNe Ic known as Type I superluminous supernovae (SLSNe) are also proposed as having similar

origins to IGRBs (e.g., Lunnan et al. 2014; Angus et al. 2016; Aguilera-Dena et al. 2018; Margalit et al. 2018), based on both theoretical and observational evidence. SLSNe exhibit intrinsic luminosities one to two orders of magnitude greater than those of “normal” SNe (see Gal-Yam 2012; Moriya et al. 2018 for reviews). Their spectral signatures point to progenitors that have undergone severe mass loss and/or mixing phases (Mazzali et al. 2016; Gal-Yam 2019), while their extreme luminosities suggest a source of power in addition to the radioactive decay of  $^{56}\text{Ni}$  that powers other SNe. Stars that have undergone CHE but failed to form BHs, instead leaving behind millisecond magnetars, have been proposed as powering these SLSNe (Kasen & Bildsten 2010; Woosley 2010; Metzger et al. 2015; Nicholl et al. 2017), by continuously depositing energy into the ejecta during spindown. Self-consistent simulations of both SLSNe and IGRBs require realistic stellar models like those presented in this Letter.

Numerical studies of IGRBs (see Lazzati et al. 2015 for a review) often manually inject a jet near the center of a stellar profile, then follow its evolution to calculate observables like light curves and spectral signatures. Alternatively, simulations can capture the ab initio engine formation, but they are then computationally limited to following the jet for too short a duration to extract observable properties (e.g., Burrows et al. 2007; Mösta et al. 2014; Halevi & Mösta 2018; Obergaulinger & Aloy 2020). Many of these numerical studies (e.g., Morsony et al. 2007; Lazzati et al. 2012; López-Cámara et al. 2013, 2016; Barnes et al. 2018; Xie & MacFadyen 2019) use pre-collapse W-R stellar models as their IGRB progenitors, most commonly the 16TI model of Woosley & Heger (2006). The choices of these stellar models assume that the process that leads to BH or protomagnetar formation leaves the rest of the star unaffected.

Recent 3D general-relativistic magnetohydrodynamical (GRMHD) simulations (Gottlieb et al. 2022a, 2022b) have been the first to self-consistently launch a jet through accretion onto a Kerr BH and follow its journey through the stellar envelope, spanning the large spatial and temporal ranges necessary to study the observable jet properties. By exploring a range of stellar density profiles represented by analytic power laws, rather than simply assuming a fit to 16TI, these simulations have shown that the steepness of the density profile constrains the physical properties of the jet (Gottlieb et al. 2022a). In particular, Gottlieb et al. (2022a) find that only those profiles that are significantly shallower than 16TI and other similar pre-collapse W-R stars are compatible with observations of IGRBs.

In this Letter, we investigate the core-collapse process in massive stripped-envelope stars, which are the likely progenitors of IGRBs, and their post-collapse properties. In Section 2, we describe the properties of the stellar models from Modules for Experiments in Stellar Astrophysics (MESA) that we evolve and our numerical setup for doing so. We report the results from our core-collapse GRID simulations, including the natures of the compact remnants and density profiles, in Section 3. We end by discussing the consequences of these results in the context of IGRBs and by encouraging future models to use physically motivated post-core-collapse stellar profiles in Section 4.

## 2. Methods

In this work, we present the results from simulations of core collapses of massive stars, and we investigate their evolution and final post-collapse states.

### 2.1. Pre-collapse Stellar Models

The initial conditions for our core-collapse simulations are drawn from the stellar evolution models described in Aguilera-Dena et al. (2020; hereafter, AD20).

AD20 present the evolution, until the onset of core collapse, of stellar progenitors of massive low-metallicity stars, spanning zero-age main-sequence (ZAMS) masses of  $M_{\text{ZAMS}} = (4\text{--}45)M_{\odot}$ . The models are computed using the open-source 1D stellar evolution MESA, version 10398 (Paxton et al. 2011, 2013, 2015, 2018). Each star is initialized with a rapid equatorial rotational velocity of  $600 \text{ km s}^{-1}$  and a low metallicity of  $(1/50)Z_{\odot}$ , where  $Z_{\odot}$  represents the solar metallicity, with abundances scaled from Grevesse et al. (1996). The fast initial rotation guarantees effective mixing, leading to quasi-CHE. These stellar models, which result in fast-rotating pre-collapse cores with hydrogen- and helium-depleted envelopes, have been proposed as potential progenitors of IGRBs and SLSNe (Aguilera-Dena et al. 2018, AD20) or SNe Ic-bl.

We evolve seven different models from the set of 42 included in AD20, spanning a range of initial masses and expected explosion properties. We choose the  $M_{\text{ZAMS}} = 18M_{\odot}$  model as our fiducial model, because it is closest in mass, at the onset of core collapse, to the well-studied IGRB progenitor model 16TI of Woosley & Heger (2006). By the start of the core-collapse process, this model has a mass of  $14.15M_{\odot}$  (compared to  $13.95M_{\odot}$  for 16TI). We note that the mass loss in the AD20 suite of models is dictated by rotation and enhanced by neutrino-driven contraction, while the 16TI model loses mass due to W-R winds. The true nature and rate of the mass loss in such low-metallicity rapidly rotating stars has been debated, as their winds may not be sufficiently optically thick to qualify as W-R stars (e.g., Szécsi et al. 2015; Shenar et al. 2020).

The  $M_{\text{ZAMS}} = 18M_{\odot}$  stellar model is classified by AD20 as a likely failed SN and potential IGRB progenitor, based on various explosion criteria. The simplest of these is the core-compactness parameter,  $\xi_M$ , which is motivated by hydrodynamic simulations of neutrino-driven SNe and defined as

$$\xi_M = \frac{M/M_{\odot}}{R(M)/1000 \text{ km}}, \quad (1)$$

where  $R(M)$  is the radius of the enclosed baryonic mass  $M$  (O’Connor & Ott 2011). This single-parameter estimate is commonly used as an indicator of “explodability”—whether or not a nonrotating stellar core will lead to a successful neutrino-driven explosion. It is often measured at a mass coordinate of  $2.5 M_{\odot}$ , which corresponds to a typical infall velocity of  $1000 \text{ km s}^{-1}$ . Successful explosions of nonrotating cores with  $\xi_{2.5} \gtrsim 0.45$  are predicted to be difficult, as calibrated by core-collapse simulations (Sukhbold & Woosley 2014). Our fiducial model has  $\xi_{2.5} = 0.62$ . All of the models we present here, except for the least massive one ( $M_{\text{ZAMS}} = 13M_{\odot}$ ), have compactness parameters above 0.45, and they are therefore

expected by this simple explodability predictor to fail to explode, instead collapsing to form BHs.

Figure 1 shows radial profiles of the density, temperature, radial velocity, and angular velocity at the onset of core collapse for the fiducial  $M_{\text{ZAMS}} = 18M_{\odot}$  model as well as the other six models. We include the initial parameters for each of these models, as taken from AD20, in the first few columns of Table 1. In particular, we list the stellar mass at the onset of core collapse (defined as the time when the core infall velocities first exceed  $1000 \text{ km s}^{-1}$ )  $M_{\text{pre-cc}}$  and the compactness parameter  $\xi_{2.5}$ . We note that while there are many similarities between the different models, there are also nonlinear differences between them—in the rotational velocities of their core regions, for example (see Figure 1(d)). This nonlinearity is also reflected in the nonmonotonic (as a function of stellar mass) behavior of  $\xi_{2.5}$ .

Besides the  $M_{\text{ZAMS}} = 13M_{\odot}$  model, all of the models that we adopt fail to meet the explosion criterion of Müller et al. (2016), which predicts the properties of neutrino-driven explosions based on a semi-analytic model of stellar structure. Both the least ( $13M_{\odot}$ ) and the most massive ( $45M_{\odot}$ ) models are predicted to explode based on the Ertl et al. (2016) test, which employs a two-parameter representation of stellar structure, while the rest fail to meet this criterion as well. These predictions are also not monotonically dependent on the initial or pre-collapse mass, due to the complexities of stellar evolution. We include the  $M_{\text{ZAMS}} = 13M_{\odot}$  model as a comparison point for the failed SNe, but we focus on the more massive models, from the perspective of likely IGRB progenitors.

## 2.2. Core-collapse Simulations

As we discuss below, we map each of the pre-collapse models onto GR1D (O’Connor & Ott 2010), a spherically symmetric general-relativistic neutrino hydrodynamics code, in order to evolve them through the final stage of stellar evolution. GR1D is an open-source tool<sup>6</sup> for simulating stellar core collapse and BH formation. It uses a finite-volume scheme with piecewise parabolic reconstruction and a Riemann solver to evolve the discretized equations of general-relativistic hydrodynamics. It couples with microphysical tabulated equations of state (EOSs) and includes a treatment of rotation that makes it effectively 1.5D. It too is a modular code and, crucially, it implements neutrino transport in the M1 formulation (O’Connor 2015), with tabulated multi-group neutrino opacities. Spherically symmetric models can never fully capture the inherently multidimensional properties of stars (e.g., critically rotating stars are expected to be significantly oblate) and their collapse processes (e.g., Müller 2016; O’Connor & Couch 2018). However, for the purpose of approximating a collapsing star’s remnant mass and averaged radial thermodynamic profiles, GR1D is a useful and sufficient tool (e.g., O’Connor & Ott 2010, 2011; O’Connor et al. 2018). GR1D allows us to simulate the entire star, rather than collapsing only the inner region, which is critical for understanding the environment that a collimated outflow from the accreting newborn compact object must propagate through and break out of in order to power a IGRB.

The initial conditions for our GR1D simulations are the pre-collapse models of AD20. Each model is remapped from

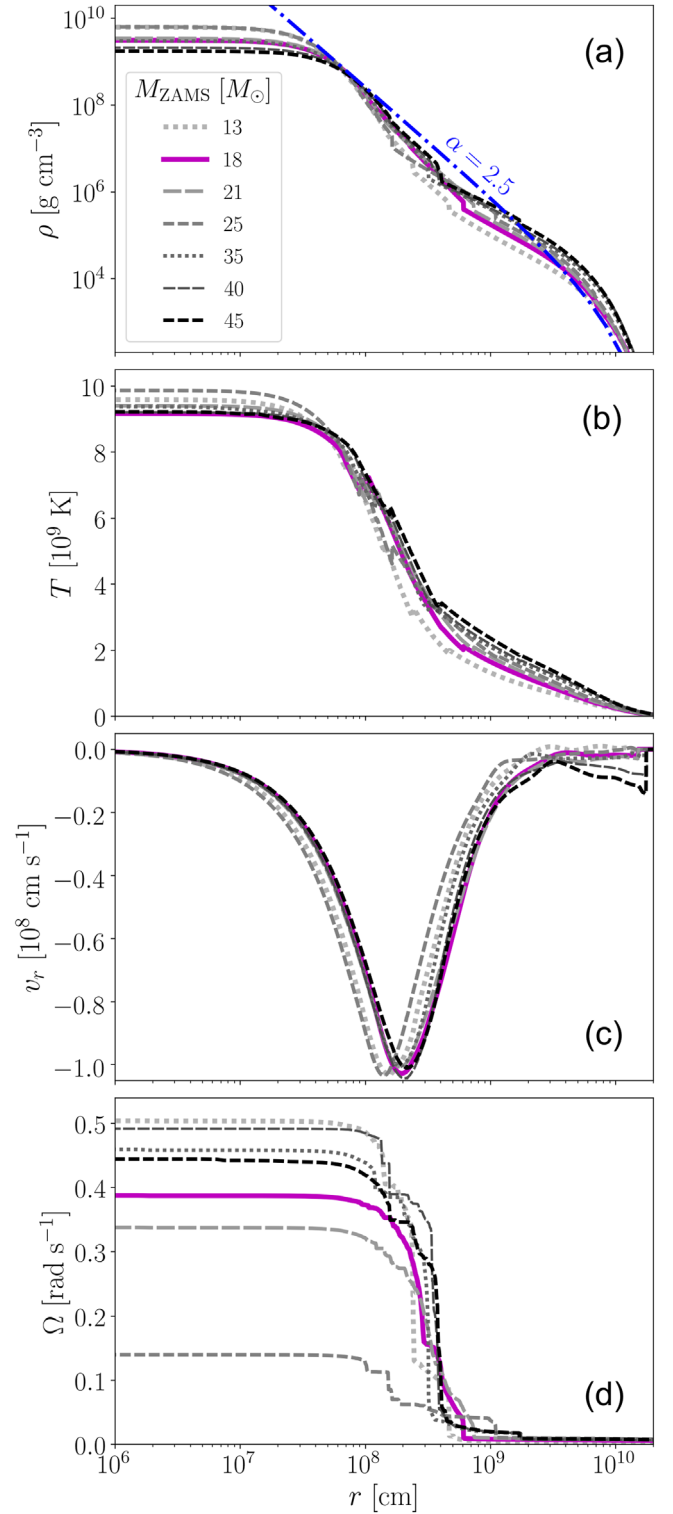


**Figure 1.** Stellar properties as functions of radius for the MESA models of AD20 at the onset of core collapse. In the four panels, we show (a) the mass density, (b) the temperature, (c) the radial velocity, and (d) the angular velocity. The different mass models are represented by the different colored and styled lines, as labeled, with the fiducial  $M_{\text{ZAMS}} = 18M_{\odot}$  model being shown in solid magenta. We also include, with the dashed–dotted blue line, a fit to Equation (2) with  $\alpha = 2.5$ , which represents the pre-collapse density profile that is characteristic of massive stellar progenitors and that has been ruled out by the observed properties of IGRBs (Gottlieb et al. 2022a). All models share similar density, temperature, and radial velocity profiles. Their core rotational velocities differ by factors of a few and vary nonmonotonically with the ZAMS mass.

<sup>6</sup> <https://github.com/evanconnor/GR1D>

**Table 1**  
Parameters of the Stellar Models

$M_{\text{ZAMS}}$ ( $M_{\odot}$ )	$M_{\text{pre-cc}}$ ( $M_{\odot}$ )	$\xi_{2.5}$	$t_{\text{bounce}}$ (ms)	$t_f$ (ms)	$M_{\text{core}}$ ( $M_{\odot}$ )	$\alpha$
13	10.37	0.21	152	835	2.03	1.42
18	14.15	0.62	234	741	2.45*	1.45
21	16.39	0.66	216	719	2.44*	1.43
25	19.33	0.47	152	767	2.08	1.37
35	26.53	0.57	247	825	2.40	1.36
40	30.08	0.78	258	735	2.68*	1.55
45	33.59	0.85	285	614	2.63*	1.44

**Note.** We take the following pre-collapse quantities directly from AD20: the ZAMS mass  $M_{\text{ZAMS}}$ ; the mass at the time of the remapping to GR1D  $M_{\text{pre-cc}}$ ; and the compactness parameter at this time  $\xi_{2.5}$ , as defined in Equation (1). We add to these the times of the core bounces in our GR1D simulations  $t_{\text{bounce}}$  and the final times at the ends of the simulations, which occur at  $t_f$ ; the mass of the inner core  $M_{\text{core}}$  (with an asterisk indicating BH formation); and the best-fit power-law index for the density profile  $\alpha$ .

MESA once it has reached a maximum core infall velocity of  $v_r > 1000 \text{ km s}^{-1}$ , representing the onset of core collapse. The masses of the stars at this time,  $M_{\text{pre-cc}}$ , are included in the third column of Table 1. In particular, we map the following parameters (as a function of radial coordinate) onto a new grid: the enclosed mass, temperature, density, radial velocity, electron fraction, and angular velocity. We choose a grid in GR1D that is uniform ( $\Delta r = 100 \text{ m}$ ) in the inner region (up to 2 km) and logarithmically spaced outside of it, with a total of 1200 radial zones (in addition to ghost zones). The grid extends out to where the density has dropped below  $\rho_{\text{min}} = 2000 \text{ g cm}^{-3}$ , corresponding to a typical radius of  $r(\rho = \rho_{\text{min}}) \approx (0.8-1) \times 10^{10} \text{ cm}$ . This value of the minimum density does not affect the evolution of the star during collapse; the grid that we use captures the overwhelming majority (>80% by mass) of each star, and the parts of the envelope at  $r \gtrsim 10^9 \text{ cm}$  ( $\rho \lesssim 10^5 \text{ g cm}^{-3}$ ) are unchanged during core collapse (see Figure 2).

We choose a commonly used tabulated EOS that is appropriate for hot nuclear matter, from Lattimer & Douglas Swesty (1991), with an incompressibility of  $K_{\text{sat}} = 220 \text{ MeV}$  (known as LS220). We include three species and 18 energy groups of neutrinos with tabulated opacities for a large parameter space of thermodynamic quantities, generated through the open-source neutrino interaction library NuLib.<sup>7</sup>

### 3. Results

#### 3.1. Core-collapse Evolution

The fiducial  $M_{\text{ZAMS}} = 18M_{\odot}$  model as well as the  $M_{\text{ZAMS}} = 21, 40, \text{ and } 45 M_{\odot}$  ones all collapse to form BHs. Every model in this set follows a similar evolution. On the other hand, the  $M_{\text{ZAMS}} = 13, 25, \text{ and } 35 M_{\odot}$  models all fail to form BHs over the duration of the simulation, so these models may be representative of successful neutrino-driven SN explosions. To represent these two different outcomes, we show the density and radial velocity profiles for the  $M_{\text{ZAMS}} = 18$  and  $13 M_{\odot}$  models at multiple stages of their evolution in Figure 2.

During collapse, the outer envelope of the star ( $r \gtrsim 4 \times 10^{10} \text{ cm}$ ) is largely unaffected, due to causality, while the inner region falls inward, making the core increasingly compact. Nuclear and strong forces in the dense core lead to the production of a proto-neutron star (PNS) and drive a shock outward at time  $t_{\text{bounce}}$  (known as core bounce). We include snapshots from just before and just after this time in Figure 2.

At  $t < t_{\text{bounce}}$ , the infalling material steepens into a shock, and there is a sharp drop in the density outside the core and a correspondingly sharp negative velocity at the same radius ( $r \approx 10 \text{ km}$ ). At  $t > t_{\text{bounce}}$ , the shock moves outward, as neutrinos are released in the core and heat the region behind it. This is reflected in the positive velocities at the boundary of the newly formed PNS and then in the outward movement of the shock.

Eventually, however, the shock stalls and falls back, leading to the infall of the shock, as seen in Figure 2 for the  $M_{\text{ZAMS}} = 18$  and  $13 M_{\odot}$  models. For the former, our fiducial model, core bounce occurs at  $t_{\text{bounce}} = 234 \text{ ms}$ . Approximately half a second later, the PNS itself begins to collapse, to form a BH, marking the end of the simulation. This is reflected in the rapid increase of the density in the inner regions within and the negative radial velocities at the PNS boundary at  $\sim 10 \text{ km}$ , where the initial shock formed at time  $t_{\text{bounce}}$ . We end our simulations at this time, because GR1D can no longer evolve the metric once the central density exceeds a certain level (dependent on the choice of metric). We list the times of the core bounce  $t_{\text{bounce}}$  and the final simulation times  $t_f$  for all models in Table 1.

#### 3.2. Compact Remnants

The central density as a function of time after the core bounce is shown for each simulation in the top panel of Figure 3. For all models, the core density grows steadily after the bounce, as the core continues to accrete mass. The cores of the  $M_{\text{ZAMS}} = 18M_{\odot}, 21M_{\odot}, 40M_{\odot}, \text{ and } 45M_{\odot}$  models all accrete enough matter to experience the runaway gravitational collapse of the PNS. At this point, the central density rises exponentially, as the core mass exceeds the maximum allowed NS mass, which is set by the EOS and the core angular momentum. At this stage, which indicates the onset of BH formation, the GR1D simulation ends, as it cannot continue to evolve the metric to a true singularity.

In each of our seven models, a shock wave is driven outward from the core at the time of the core bounce. However, it stalls and turns back within 100 ms for all models, as fallback accretion occurs. The  $M_{\text{ZAMS}} = 13$  and  $25 M_{\odot}$  models both experience brief shock revivals powered by neutrino heating, but still eventually undergo reversals and fallback accretion, as seen in the inset in the middle panel of Figure 3. These two models also have the least enclosed mass within the shock radius and the lowest pre-collapse compactness parameters (see Table 1).

The  $M_{\text{ZAMS}} = 35M_{\odot}$  model also fails to collapse to a BH by the end of the simulation. These outcomes suggest a critical core-compactness parameter of  $\xi_{2.5} \approx 0.6$ , with models that are more compact than this value collapsing to BHs in our GR1D simulations. However, it is possible that in longer or multidimensional simulations, some of the models that we do not see collapsing in GR1D would do so. This is especially likely for the  $M_{\text{ZAMS}} = 35M_{\odot}$  model, which has the most massive core (as seen in Table 1 as well as the bottom panel of

<sup>7</sup> <http://www.nulib.org/>

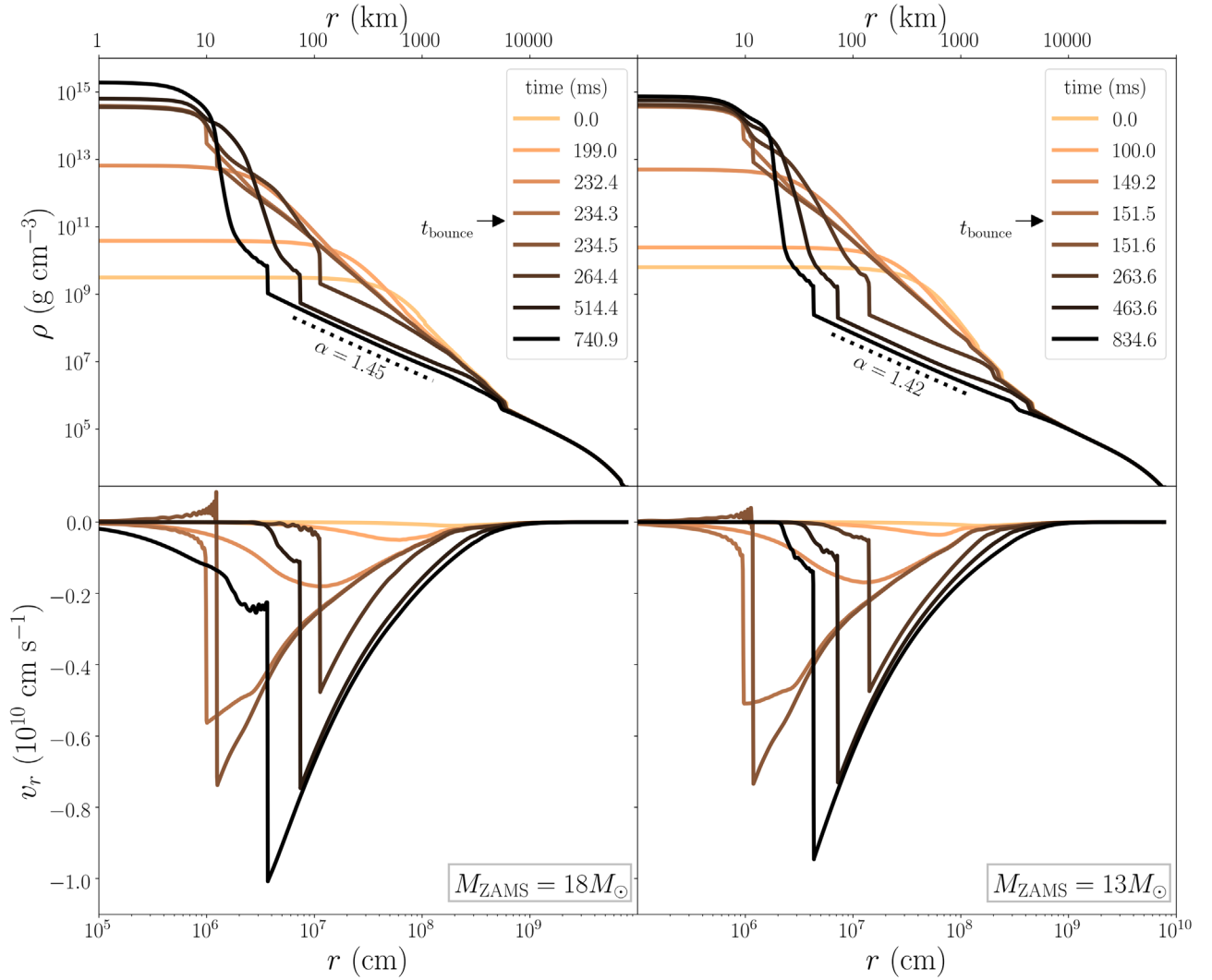


**Figure 2.** Evolutions of the density and velocity profiles (in the top and bottom panels, respectively) of the  $M_{\text{ZAMS}} = 18M_{\odot}$  and  $13M_{\odot}$  models (left and right, respectively), during the GR1D evolutions through core collapse. The density profiles evolve similarly for both models, significantly flattening after the shock stalls. In the bottom left panel, there is infall within the core (at  $r < 10^6$  cm) in the final snapshot for the  $18M_{\odot}$  model, but there is no such infall in the final state of the  $13M_{\odot}$  model. This is evidence that the core of the  $18M_{\odot}$  model collapses to a BH at the end of its evolution, whereas the core of the  $13M_{\odot}$  model remains a PNS.

Figure 3) and the greatest pre-collapse compactness parameter (0.57) of the non-BH-forming models.

The inner core mass  $M_{\text{core}}$  is defined as the mass within the radius at which the radial velocity first exceeds the sound speed,  $r_{\text{shock}}$ . While  $M_{\text{core}}$  increases throughout the duration of our simulations, the rate at which it does so decreases for all models, as the accretion slows and  $r_{\text{shock}}$  asymptotes. Each model forms a core of mass  $2M_{\odot} < M_{\text{core}} < 2.7M_{\odot}$  by the end of its simulation, as shown in both Table 1 and the bottom panel of Figure 3. In all cases,  $M_{\text{core}}$  represents a lower limit on the baryonic mass of the final remnant, under the assumptions of spherical symmetry (with effective rotation) and purely neutrino-hydrodynamical evolution. The true final remnant masses may be larger, as accretion continues slowly at the end of the GR1D simulations, and they may differ with the inclusion of multidimensional and/or magnetic effects when simulating the core-collapse evolution.

### 3.3. Density Profiles

For each of the seven simulations, we find that the density profile after core collapse is well fit by a distribution of the

form

$$\rho(r) = \rho_0 \left( \frac{r}{r_g} \right)^{-\alpha} \left( 1 - \frac{r}{R_{\star}} \right)^3, \quad (2)$$

where  $\rho_0$  is the normalization factor satisfying  $M_{\star} = \int_0^{R_{\star}} \rho(r) dV$ ,  $r_g$  is the gravitational radius of the remnant, and  $R_{\star}$  is the stellar radius.

The initial density profiles are similar across stellar masses, with a best-fit power-law index of  $\alpha \approx 2.5$ . In all cases, the density profile becomes shallower during core collapse, and especially after the shock stalls and turns around. The final density and pressure profiles are very smooth in the region  $20 \text{ km} \lesssim r \lesssim 2000 \text{ km}$ . For our fiducial collapsed stellar model at the end of the GR1D simulation, we find a best-fit value of  $\alpha = 1.45$  for the density outside the BH event horizon. We include the best-fit values of  $\alpha$  for all models in the final column of Table 1. They vary nonmonotonically with mass, though clearly trend steeper for higher values of core compactness  $\xi_{2.5}$ , ranging from 1.36 for the  $M_{\text{ZAMS}} = 35M_{\odot}$  model to 1.55 for the  $M_{\text{ZAMS}} = 40M_{\odot}$  model. We compare the

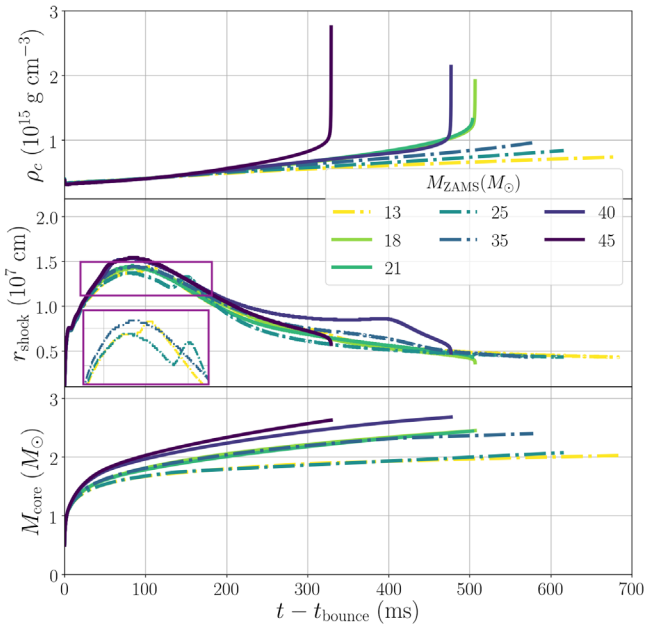


**Figure 3.** Evolutions of several key quantities (from top to bottom: the central density, shock radius, and mass of the inner core) with time after the core bounce for all seven models. The shock radius  $r_{\text{shock}}$  is defined as the place where the radial velocity exceeds the sound speed and the inner core is the region within this radius, so  $M_{\text{core}} \equiv M(r < r_{\text{shock}})$ . Models that form BHs in our simulations are represented by solid lines, while models that do not are shown by dashed–dotted lines. The inset in the middle panel zooms in on the shock radius evolutions for the three models that do not form BHs, two of which experience a brief shock revival stage.

density profiles for all seven models at the beginnings and ends of their GR1D simulations in Figure 4. Outside the cores, at radii  $r > r_{\text{shock}}$ , the density distributions are very similar in shape across all models.

#### 4. Discussion and Conclusion

Power-law density profiles with indices of  $\alpha \approx 1.5$  are consistent with the simple case of freefall acceleration outside the core. This makes it all the more meaningful that the GR1D simulations that we perform yield this robust result for the final states of all models. The initial models have nonlinear differences in their stellar structure, so there are complicated variations in the inputs to GR1D. These differences are mainly related to whether core carbon burning proceeds radiatively or convectively.

Meanwhile, the physics that enters these 1D simulations is complex, in that we simulate collapse in full general relativity, with multi-group neutrino transport and realistic tabulated EOSs that are suitable for dense matter. Simulations that do not include neutrino transport produce dramatically different results, with post-collapse density profiles that are significantly steeper, reflecting the pre-collapse state. This suggests that the neutrinos radiated from the core play an important role in shaping the thermodynamic evolution of the stellar envelope. The superficially simple outcome that we find—that post-collapse stellar profiles outside the PNS or BH closely approximate those predicted by freefall acceleration—is thus all the more surprising.

We note that for the set of models that we evolve, there is a slight positive correlation between the core compactness  $\xi_{2.5}$  and the steepness of the final density profile. It remains to be seen whether this holds for a broader range of stellar evolution

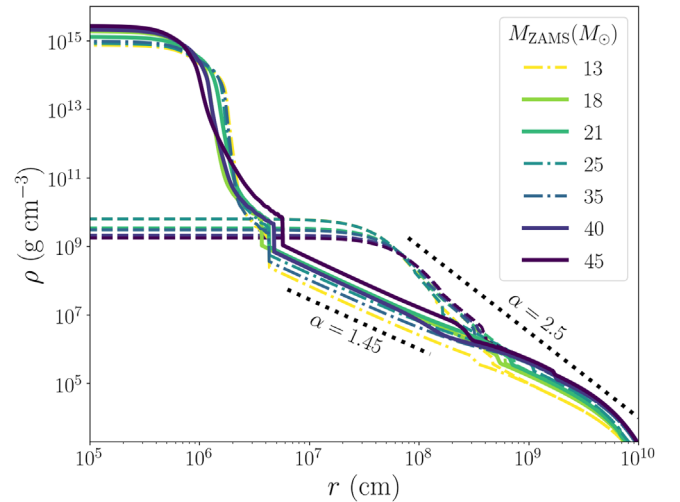


**Figure 4.** Initial (pre-core-collapse) and final density profiles for all seven stellar models. The initial profiles are shown by the dashed lines. For the final profiles, we use solid lines for the models that collapse to form BHs in our simulations and we use dashed–dotted lines for those that do not. Representative power-law scalings are shown by dotted black lines, for comparison. While all pre-collapse stellar models have steep density profiles ( $\alpha \approx 2.5$ ), all post-collapse profiles are shallow ( $\alpha \approx 1.45$ ). Stellar models that are initially inconsistent with IGRB observables evolve robustly to the post-collapse state that is necessary for jet properties that are consistent with observations, showing that massive stars that have undergone CHE are likely IGRB progenitors under the collapsar model.

models, rather than only for those with low metallicities and rapid rotation that experience wind-driven mass loss and significant mixing, as is typical of IGRB progenitors.

#### 4.1. Applications for IGRBs

The consequences of the shallow density profiles that we find in our 1D core-collapse simulations of real stellar progenitor models are favorable for producing IGRBs. 3D GRMHD simulations of collapsars have followed the formation, propagation, and breakout of jets (Gottlieb et al. 2022a, 2022b). These simulations begin with idealized initial conditions of a central BH that is surrounded by an effectively zero-temperature star, represented by an analytic power-law density profile as in Equation (2). Dipolar magnetic fields and fast rotational velocities are then added to the idealized stellar profile, leading to disk accretion, a buildup of magnetic flux at the BH event horizon, and the launching of a jet that propagates through the stellar envelope. Gottlieb et al. (2022a) varied the initial power-law index  $\alpha$  and compared the physical quantities that were inferred from the resulting jets to observational constraints. They concluded that inner stellar density profiles with indices of  $0.5 \lesssim \alpha \lesssim 1.5$  may be responsible for producing the full range of IGRB observables. In particular, such profiles were found to be necessary to produce jets with the proper luminosities as well as the proper (flat) evolution of jet power with time. On the other hand, the density profiles of the pre-collapse model 16TI (Woosley & Heger 2006) and the pre-collapse models of AD20 are steeper, with  $\alpha \approx 2.5$ . Such profiles would require an unrealistically high jet luminosity to overcome accretion and break out,  $L_{\text{jet}} \gtrsim 10^{52} \text{ erg s}^{-1}$ . They also produce time-evolving accretion rates, which in turn translate to evolving jet luminosities (Gottlieb et al. 2022a). Both of these properties would be in tension with the observations of IGRBs.

Here, we have shown that commonly used pre-collapse IGRB progenitor models (e.g., 16TI of Woosley & Heger 2006) with density profiles that have power-law indices of  $\alpha \approx 2.5$  naturally lead to post-collapse profiles with  $\alpha \lesssim 1.5$ . The density profiles, while flattened during the collapse in the inner region of each star, are largely unchanged outside a radius of  $r \gtrsim 3\text{--}5 \times 10^8$  cm. Numerical studies that inject jets through an inner boundary with a radius of several thousand kilometers are thus justified in using pre-collapse stellar profiles as the background state through which such jets propagate.

A limitation of this result is that a subset of our stellar models may successfully explode as SNe, either through the standard neutrino-driven mechanism (mainly for the  $M_{\text{ZAMS}} = 13, 35M_{\odot}$  models) or magnetorotationally, when simulated in multiple dimensions with magnetic fields and rotation. The general-relativistic neutrino-hydrodynamical 1D simulations that we present here do not produce SNe, so we are unable to capture the possible effects of such explosions on the resultant density profiles. Simulating the explosion process is beyond the scope of this work and outside the capabilities of GR1D, but potentially important for ensuring that the stellar profiles that are used in IGRB simulations are fully consistent with the expectations relating to their corresponding progenitor models, which may yield SNe. To address this limitation, we plan to perform 3D GRMHD core-collapse simulations to verify the final density profiles that we obtain in the case of multidimensional and magnetic effects.

Another caveat is that we do not consider the possibility of a jet being driven by the PNS before BH formation. In the case of such a precursor jet, the density profile may be modified at the time of the IGRB jet launching. However, we cannot simulate this process with the techniques used here and do not require the existence of a precursor jet to produce a successful BH-driven jet. The results of Gottlieb et al. (2022b), which assume a power-law density profile with  $\alpha = 1.5$ , confirm that despite the strong mixing with the star leading to the baryon loading of the BH-driven jet early on, it is still able to remain intact and pierce through the envelope. As it does so, the BH-driven jet retains its energy and relativistic velocity, generating a typical IGRB, without needing to invoke a precursor jet. The stellar progenitor models that we include in this work have post-collapse density profiles akin to those chosen by Gottlieb et al. (2022b), which are expected to result in similarly promising jets. We plan to account for the possible signature of a precursor jet by considering spherically asymmetric density profiles in 3D GRMHD simulations.






In future work, we will present results from 3D GRMHD simulations that self-consistently capture jet launching, propagation, and breakout through the fiducial post-collapse stellar profile presented here, with realistic thermodynamic properties (G. Halevi et al. 2023, in preparation). We emphasize that for consistency and physical accuracy, future numerical studies and theoretical models of IGRBs should consider post-collapse stellar models as the material through which IGRB jets evolve.

We thank Evan O’Connor for helpful discussions and advice about using GR1D. We also thank Jim Stone, Eliot Quataert, and Elias Most for helpful discussions, and the anonymous referee for insightful feedback on an earlier version of this manuscript. G.H. is supported in part by a National Science Foundation Graduate Research Fellowship. O.G. is supported by a CIERA Postdoctoral Fellowship. O.G. and A.T.

acknowledge support from the Fermi Cycle 14 Guest Investigator program 80NSSC22K0031. A.T. was supported by NSF grant Nos. AST-2107839, AST-1815304, AST-1911080, and OAC-2031997, and NASA grant No. 80NSSC18K0565. D.R.A.-D. acknowledges support from the Stavros Niarchos Foundation (SNF) and the Hellenic Foundation for Research and Innovation (HFRI) under the 2nd Call for Action “Science and Society” “Always Strive for Excellence—Theodoros Papazoglou” (Project No. 01431). The simulations presented here were performed on computational resources that are managed and supported by Princeton Research Computing, a consortium of groups including the Princeton Institute for Computational Science and Engineering (PICSciE) and the Office of Information Technology’s High Performance Computing Center and Visualization Laboratory at Princeton University.

*Software:* GR1D (O’Connor & Ott 2010; O’Connor 2015), Matplotlib (Hunter 2007).

## ORCID iDs

Goni Halevi  <https://orcid.org/0000-0002-7232-101X>  
 Philipp Mösta  <https://orcid.org/0000-0002-9371-1447>  
 Ore Gottlieb  <https://orcid.org/0000-0003-3115-2456>  
 Alexander Tchekhovskoy  <https://orcid.org/0000-0002-9182-2047>  
 David R. Aguilera-Dena  <https://orcid.org/0000-0002-3874-2769>

## References

- Aguilera-Dena, D. R., Langer, N., Antoniadis, J., & Muller, B. 2020, *ApJ*, **901**, 114
- Aguilera-Dena, D. R., Langer, N., Antoniadis, J., et al. 2022, *A&A*, **661**, A60
- Aguilera-Dena, D. R., Langer, N., Moriya, T. J., & Schootemeijer, A. 2018, *ApJ*, **858**, 115
- Angus, C. R., Levan, A. J., Perley, D. A., et al. 2016, *MNRAS*, **458**, 84
- Barnes, J., Duffell, P. C., Liu, Y., et al. 2018, *ApJ*, **860**, 38
- Blandford, R. D., & Znajek, R. L. 1977, *MNRAS*, **179**, 433
- Bloom, J. S., Kulkarni, S. R., & Djorgovski, S. G. 2002, *AJ*, **123**, 1111
- Burrows, A., Dessart, L., Livne, E., Ott, C. D., & Murphy, J. 2007, *ApJ*, **664**, 416
- Dessart, L., John Hillier, D., Yoon, S.-C., Waldman, R., & Livne, E. 2017, *A&A*, **603**, A51
- Eisenberg, M., Gottlieb, O., & Nakar, E. 2022, *MNRAS*, **517**, 582
- Ertl, T., Janka, H.-T., Woosley, S. E., Sukhbold, T., & Ugliano, M. 2016, *ApJ*, **818**, 124
- Galama, T. J., Vreeswijk, P. M., van Paradijs, J., et al. 1998, *Natur*, **395**, 670
- Gal-Yam, A. 2012, *Sci*, **337**, 927
- Gal-Yam, A. 2019, *ApJ*, **882**, 102
- Gal-Yam, A., Arcavi, I., Ofek, E. O., et al. 2014, *Natur*, **509**, 471
- Gottlieb, O., Lalakos, A., Bromberg, O., Liska, M., & Tchekhovskoy, A. 2022a, *MNRAS*, **510**, 4962
- Gottlieb, O., Liska, M., Tchekhovskoy, A., et al. 2022b, *ApJL*, **933**, L9
- Grevesse, N., Noels, A., & Sauval, A. J. 1996, in ASP Conf. Ser. 99, Cosmic Abundances, ed. S. S. Holt & G. Sonneborn (San Francisco, CA: ASP), 117
- Halevi, G., & Mösta, P. 2018, *MNRAS*, **477**, 2366
- Hunter, J. D. 2007, *CSE*, **9**, 90
- Kasen, D., & Bildsten, L. 2010, *ApJ*, **717**, 245
- Komissarov, S. S., & Barkov, M. V. 2009, *MNRAS*, **397**, 1153
- Lattimer, J. M., & Douglas Swesty, F. 1991, *NuPhA*, **535**, 331
- Lazzati, D., Morsony, B. J., Blackwell, C. H., & Begelman, M. C. 2012, *ApJ*, **750**, 68
- Lazzati, D., Morsony, B. J., & López-Cámara, D. 2015, *JHEAp*, **7**, 17
- López-Cámara, D., Lazzati, D., & Morsony, B. J. 2016, *ApJ*, **826**, 180
- López-Cámara, D., Morsony, B. J., Begelman, M. C., & Lazzati, D. 2013, *ApJ*, **767**, 19
- Lunnan, R., Chornock, R., Berger, E., et al. 2014, *ApJ*, **787**, 138
- MacFadyen, A. I., & Woosley, S. E. 1999, *ApJ*, **524**, 262

- Margalit, B., Metzger, B. D., Thompson, T. A., Nicholl, M., & Sukhbold, T. 2018, *MNRAS*, **475**, 2659
- Mazzali, P. A., Sullivan, M., Pian, E., Greiner, J., & Kann, D. A. 2016, *MNRAS*, **458**, 3455
- Metzger, B. D., Giannios, D., Thompson, T. A., Bucciantini, N., & Quataert, E. 2011, *MNRAS*, **413**, 2031
- Metzger, B. D., Margalit, B., Kasen, D., & Quataert, E. 2015, *MNRAS*, **454**, 3311
- Modjaz, M., Liu, Y. Q., Bianco, F. B., & Graur, O. 2016, *ApJ*, **832**, 108
- Modjaz, M., Stanek, K. Z., Garnavich, P. M., et al. 2006, *ApJL*, **645**, L21
- Moriya, T. J., Sorokina, E. I., & Chevalier, R. A. 2018, *SSRv*, **214**, 59
- Morsony, B. J., Lazzati, D., & Begelman, M. C. 2007, *ApJ*, **665**, 569
- Mösta, P., Richers, S., Ott, C. D., et al. 2014, *ApJL*, **785**, L29
- Müller, B. 2016, *PASA*, **33**, e048
- Müller, B., Heger, A., Liptai, D., & Cameron, J. B. 2016, *MNRAS*, **460**, 742
- Nicholl, M., Guillochon, J., & Berger, E. 2017, *ApJ*, **850**, 55
- Obergaulinger, M., & Aloy, M. A. 2020, *MNRAS*, **492**, 4613
- O'Connor, E. 2015, *ApJS*, **219**, 24
- O'Connor, E., Bollig, R., Burrows, A., et al. 2018, *JPhG*, **45**, 104001
- O'Connor, E., & Ott, C. D. 2010, *CQGra*, **27**, 114103
- O'Connor, E., & Ott, C. D. 2011, *ApJ*, **730**, 70
- O'Connor, E. P., & Couch, S. M. 2018, *ApJ*, **865**, 81
- Paxton, B., Bildsten, L., Dotter, A., et al. 2011, *ApJS*, **192**, 3
- Paxton, B., Cantiello, M., Arras, P., et al. 2013, *ApJS*, **208**, 4
- Paxton, B., Marchant, P., Schwab, J., et al. 2015, *ApJS*, **220**, 15
- Paxton, B., Schwab, J., Bauer, E. B., et al. 2018, *ApJS*, **234**, 34
- Shankar, S., Mösta, P., Barnes, J., Duffell, P. C., & Kasen, D. 2021, *MNRAS*, **508**, 5390
- Shenar, T., Gilkis, A., Vink, J. S., Sana, H., & Sander, A. A. C. 2020, *A&A*, **634**, A79
- Song, C.-Y., & Liu, T. 2023, arXiv:2301.05401
- Sukhbold, T., & Woosley, S. E. 2014, *ApJ*, **783**, 10
- Szécsi, D., Langer, N., Yoon, S.-C., et al. 2015, *A&A*, **581**, A15
- Woosley, S. E. 1993, *ApJ*, **405**, 273
- Woosley, S. E. 2010, *ApJL*, **719**, L204
- Woosley, S. E., & Heger, A. 2006, *ApJ*, **637**, 914
- Xie, X., & MacFadyen, A. 2019, *ApJ*, **880**, 135